APL Materials

RESEARCH ARTICLE | SEPTEMBER 23 2025

Molecular beam epitaxy growth of IrO_2 using plasma-only oxidation

D. Sacksteder ; S. C. Dahl ; J. Dorsey ; K. Yazawa ; M. E. Holtz

APL Mater. 13, 091117 (2025)
https://doi.org/10.1063/5.0282709

APL Materials ARTICLE pubs.aip.org/aip/apm

Molecular beam epitaxy growth of IrO_2 using plasma-only oxidation

Cite as: APL Mater. 13, 091117 (2025); doi: 10.1063/5.0282709
Submitted: 27 May 2025 • Accepted: 6 September 2025 •
Published Online: 23 September 2025

D. Sacksteder,[1] S. C. Dahl,[1] J. Dorsey,[1] K. Yazawa,[1,2] and M. E. Holtz[1,a)]

AFFILIATIONS

[1] Colorado School of Mines, Golden, Colorado 80401, USA
[2] National Renewable Energy Laboratory, Golden, Colorado 80401, USA

[a)] **Author to whom correspondence should be addressed:** mholtz@mines.edu

ABSTRACT

Growth of IrO_2 films via molecular beam epitaxy (MBE) using an oxygen plasma as the sole oxidant is demonstrated for the first time. We investigate the oxidizing conditions required for IrO_2 by characterizing the species present in the plasma using optical emission spectroscopy and comparing the thermodynamic equilibrium between Ir/IrO_2 under atomic and molecular oxygen. Across the pressure range accessible, monatomic oxygen was the primary reactive species present in the plasma. IrO_2 films were grown under varying Ir flux, oxygen pressure, and substrate temperature to understand growth thermodynamics and kinetics. Structural characterization assessed film phase and composition, crystallinity, strain, and surface morphology. The optimized films from this study validate plasma-only reactive growth by MBE as a successful method for growing IrO_2.

I. INTRODUCTION

Iridium oxide in the rutile crystal structure ($P4_2/mnm$) is of interest to a variety of specialties spanning electronics,[1–4] biomedicine,[5,6] catalysis,[7–10] superconductivity,[8,11,12] and spin applications.[8,13–17] Given this wide range of research applications, IrO_2 thin films have been synthesized in many ways, including sputtering,[1–4] atomic layer deposition,[5,6,9,18–20] chemical vapor deposition,[21] pulsed laser deposition,[22–24] chemical bath deposition,[5] sol–gel synthesis,[25] and thermal oxidation.[26] High-quality epitaxial films of iridium oxide have been grown via reactive molecular beam epitaxy (MBE) using ozone-assisted MBE (OAMBE)[8,13–16,27,28] and metal-organic MBE (MOMBE).[12,17] However, growth via plasma-assisted MBE (PAMBE) has not been documented in the literature without metal-organic sources. While the thermodynamics of IrO_2 formation from the ozone reaction are well documented,[8,13,29] the understanding of PAMBE growth is limited due to the variety of species present in plasma. Because Ir is one of the most difficult elements to oxidize,[30] the growth of IrO_2 is a good test case to establish the ability of PAMBE to produce stubborn metal-oxide films.

Here, we investigate the growth of IrO_2 films via PAMBE. We characterize the low-pressure RF oxygen plasma to identify composition as a function of pressure, verifying atomic oxygen as the primary oxidizing species. Ellingham diagrams for the Ir/IrO_2 equilibrium are calculated and compared to oxidation via O_2 and O. We demonstrate the growth of phase-pure epitaxial films of IrO_2 via PAMBE, in which the reactive species from the RF plasma are the sole oxidants. The films are characterized for structural and chemical quality using atomic force microscopy (AFM), x-ray diffraction (XRD), and scanning transmission electron microscopy (STEM) to investigate the crystalline quality. The results of this study establish that atomic oxygen from an RF plasma source is oxidizing enough to form IrO_2 within the MBE growth pressure regime.

II. EXPERIMENTAL

We used optical emission spectroscopy (OES) to verify the composition of the plasma used during reactive growth. The plasma was characterized at three pressures (3.8×10^{-5}, 5.5×10^{-5}, and 7.6×10^{-5} mbar), corresponding approximately to the three pressures at which samples were grown. A fiber optic cable was positioned perpendicular to the viewport built into the plasma source to collect a signal, as described elsewhere.[31] All spectra were collected using a spectrometer with 0.5 nm resolution. Sixty spectra for each

pressure condition were collected between 200 and 1100 nm with an integration time of 1 s and averaged to improve the signal-to-noise ratio, which degraded at higher pressures due to higher background signals. Peaks were analyzed using the National Institute of Standards and Technology (NIST) Atomic Spectra Database.[32]

The equations for the phase equilibria used to construct the Ellingham diagram were derived according to the treatment previously described in the literature.[29,30,33] The Gibbs free energy of formation for atomic oxygen was obtained by performing a linear regression on data from the NIST JANAF Database.[34] The phase boundaries for the two reactions were compared to the operable regime of our MBE chamber to select different growth conditions for this study.

All films were grown using an oxide MBE chamber equipped with an electron-beam evaporator to supply Ir flux and a 13.56 MHz RF plasma source and matching network to supply atomic oxygen. The RF source was supplied with 250 W to spark a plasma. Different O_2 flow rates were regulated with a mass flow controller to achieve different background pressures for growth between 4.1×10^{-5} and 7.2×10^{-5} mbar. A quartz crystal monitor (QCM) was used to maintain a consistent flux of Ir from the electron beam evaporator during growth. All films were grown on Nb:TiO_2 (110) substrates from Shinkosha Co. Ltd., Kanagawa, Japan. These substrates are prepared in advance by the manufacturer and do not require additional cleaning prior to growth. Films were grown at substrate temperatures of either 400 or 300 °C and cooled in O_2 to prevent the formation of oxygen vacancies.[12] Reflection high-energy electron diffraction (RHEED) was used to examine substrate and film quality *in situ* before and after deposition.

After deposition, films were assessed for phase purity, crystallinity, and epitaxial orientation using XRD. All XRD experiments were conducted with a diffractometer equipped with a Ge (220) four-bounce monochromator and a proportional detector. Phase purity was assessed with 2θ–ω scans to determine that only rutile oxide peaks and no metallic Ir peaks were present. The full width at half maximum (FWHM) of rocking curves (ω scans) was taken to determine the degree of mosaicity in the film. The diffractometer was also used to collect x-ray reflectivity (XRR) scans of the films, which serve as a measure of thickness and surface roughness. Reciprocal space maps (RSMs) were used to characterize epitaxial quality and strain in the smoothest phase-pure film.

Film topography was imaged with AFM to verify smoothness and identify any irregular features on the surface. Scans were flattened using the masked second-degree polynomial algorithm to eliminate the bowing artifact caused by the stage mechanism.[35] Root-mean-square (RMS) roughness values were calculated from 10 μm square AFM scans.

STEM was used to investigate film crystallinity and interfacial quality. Cross-sectional samples were prepared by focused ion beam lift-out with a final milling step at 2 kV. The film was imaged using an annular dark field detector; the composition was assessed using x-ray energy dispersive spectroscopy (EDS), and lattice parameters and strain were measured using scanning electron diffraction (4D-STEM). 4D-STEM data were acquired with the NanoMegas precession electron diffraction with a 0.5° precession angle and captured with a Merlin Quantum Detectors fast electron detector. The lattice parameters were extracted using the exit wave power cepstrum procedure described elsewhere.[36]

III. RESULTS AND DISCUSSION

A. OES

The results from the OES measurements demonstrated that the plasma is mainly composed of atomic oxygen species at all three pressure conditions (Fig. 1). The spectra were collected for the same duration and are not normalized to allow for comparison of peak intensity between pressure conditions. Relevant peaks and the corresponding emitting species are listed in Table I. Peaks known to be unique to atomic oxygen (unconfounded with molecular oxygen peaks or likely contaminants) are observed at 778, 844, and 1026 nm at all pressures, indicating a dissociative plasma. Ionized molecular oxygen and nitrogen are known to emit broader bands between 500 and 700 nm.[31,37–40] These are observed but not very strong in intensity, indicating that while O_2 is present in the chamber, it is generally not ionized or excited. We assume that unionized diatomic species are not significantly reactive and do not contribute to the oxidation, which is justified by the thermodynamic calculations below. The peaks at 279.5 and 409.5 nm could be caused by either atomic nitrogen or atomic oxygen species. However, because they decrease with increasing pressure, we believe these peaks were mainly caused by nitrogen contamination. The peak at 1073 nm is ascribed to argon and carbon contamination and also increases in intensity at lower pressures. Trace amounts of nitrogen, argon, and carbon are all observed in the chamber with a residual gas analyzer. We conclude that the primary *active* oxidant from the plasma source is atomic oxygen species and apply this assumption to our thermodynamic calculations.

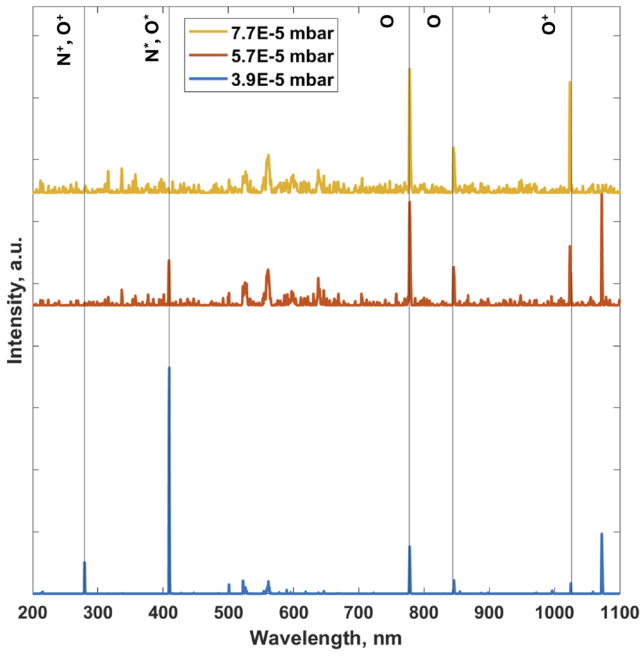

FIG. 1. OES spectra of the plasma at the three pressures used in growth. The peaks tracked in the spectra analysis are annotated.

TABLE I. Oxygen plasma OES peaks and possible species.

Wavelength, nm	Species
279.5[a]	N^+, O^+
409.5[a]	N, O[b]
525.7	O_2^+
559.1	O_2^+
561.5	O^+, C
598.2	O_2^+
636.2	O_2^+
777.5[a]	O
844[a]	O
1026[a]	O^+
1073	Ar, Ar^+, C

[a]Prominent peaks in our data.
[b]Multiple possible oxidation states.

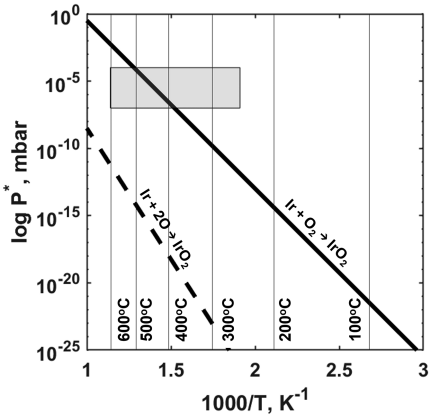

FIG. 2. Representations of the thermodynamic growth window for IrO_2 with different oxidizing species. P* corresponds to the pressure of the relevant oxidant. The relevant oxidant species is assumed to be the main oxidant in the chamber. The temperature corresponds to the substrate temperature during growth. The operable regime of the MBE system is boxed in gray for reference.

B. Thermodynamic calculations

To ascertain the MBE growth window of IrO_2, we have calculated the Ir–IrO_2 equilibrium diagrams. Although MBE growth is a non-equilibrium process, these diagrams can be instructive in identifying optimal growth windows. We consider two oxidants: molecular oxygen and atomic oxygen, and discuss how they compare to ozone, which has been studied previously. The reactions are written such that 1 mol of IrO_2 is produced in each case. The full derivation of each pressure–temperature relationship is in the supplementary material. Table II summarizes the representative chemical equation, expression for the standard Gibbs free energy of the reaction, and pressure–temperature relationship for both cases. These equilibria are plotted with respect to oxidant pressure and temperature in Fig. 2 so that the pressure on the y-axis corresponds to the partial pressure of either atomic oxygen or molecular oxygen for their respective lines. This plotting method allows us to directly compare how the required oxidant partial pressure changes with species; however, previous literature for ozone oxidation[29,41,42] instead plotted equivalence lines for ozone on a molecular oxygen pressure axis by plotting the equilibrium lines between ozone and molecular oxygen. Notably, atomic oxygen is the primary species responsible for oxidizing the film surface for both the ozone and plasma cases. The physical mechanism behind ozone oxidation includes a dissociation step: when the ozone hits the film, the O_3 dissociates into an O_2 and an O. The atomic O, as the more reactive species, is then present at the growth surface and is responsible for most of the oxidation. In the case of plasma, atomic oxygen is also the primary oxidant, but it is already formed before it hits the substrate. While the energetics and growth mechanisms between plasma and ozone are very different—the plasma contains highly energetic species while the ozone is highly reactive and dissociates—these are not captured by the thermodynamic model. Here, we use Ellingham diagrams to compare the oxidation using atomic oxygen (as produced by a plasma or by ozone dissociation) with molecular oxygen. Atomic oxygen produces many orders of magnitude easier oxidation of iridium than O_2. The thermodynamics indicate that IrO_2 is thermodynamically favored for high pressure, low temperature regions that are assessable by MBE for O and O_2, although MBE growth of IrO_2 by molecular oxygen has not been experimentally observed, indicating successful growth is also controlled by kinetics.

C. Film growth conditions and phase purity

The growth conditions for all the films in this study and a brief summary of their characteristics are presented in Table III. These conditions spanned the range of pressure–temperature conditions accessible in the MBE, as shown in Fig. 2.

A comparison of XRD $2\theta - \omega$ scans illustrates how different growth conditions affected oxidation and phase purity of the films (Fig. 3). Samples 1–3 contain Ir 111 peaks at $2\theta = 40.55^\circ$, meaning

TABLE II. Summary of equilibrium relationships for different oxidants.[a]

Chemical equation	Standard Gibbs free energy of reaction, $\Delta G^o_{rxn,\ i}(T)$ (J mol^{-1})	Pressure–temperature equilibrium expression (mbar)
$Ir + O_2 \rightarrow IrO_2$	$\Delta G^o_{rxn,\ O_2}(T) = \Delta G^o_{f,\ IrO_2}(T)$	$P_{O_2} = P_s\ \exp \frac{\Delta G^o_{rxn,\ O_2}}{RT}$
$Ir + 2O \rightarrow IrO_2$	$\Delta G^o_{rxn,\ O}(T) = \Delta G^o_{rxn,O_2}(T) - 2 * \Delta G^o_{f,O}(T)$	$P_O = P_s\ \exp \frac{\Delta G^o_{rxn,\ O}}{2RT}$

[a]$\Delta G^o_{rxn,\ O_2}(T)$ is the Gibbs free energy of oxidizing Ir with molecular oxygen. $\Delta G^o_{f,\ IrO_2}(T)$ is the Gibbs free energy of formation of IrO_2 at standard conditions. P_{O_2} is the partial pressure of molecular oxygen. P_s is the standard pressure. $\Delta G^o_{rxn,\ O}(T)$ is the Gibbs free energy of oxidizing Ir with atomic oxygen. $\Delta G^o_{f,\ IrO_2}(T)$ is the Gibbs free energy of formation of atomic oxygen at standard conditions. R is the ideal gas constant. T is the temperature.

TABLE III. Film growth conditions and summary of results.

Sample id	T, °C[a]	P, mbar[b]	Ir flux, Å/s[c]	Growth rate, Å/s[d]	Thickness, nm[d]	Phases present	Surface quality
1	400	5.1×10^{-5}	0.09	N/A	21[c]	IrO_2, Ir	Spotty RHEED
2	400	5.9×10^{-5}	0.02	0.058	17	IrO_2, Ir	Spotty RHEED
3	300	5.2×10^{-5}	0.05	0.044	28	IrO_2, Ir	Diffuse RHEED
4	300	7.3×10^{-5}	0.10	0.058	23	IrO_2	R_{RMS} = 15.36 Å, raised islands
5	300	7.0×10^{-5}	0.05	0.098	28	IrO_2	R_{RMS} = 4.08 Å
6	300	4.3×10^{-5}	0.03	0.027	13	IrO_2	R_{RMS} = 3.04 Å
7	300	5.9×10^{-5}	0.03	0.031	13	IrO_2	R_{RMS} = 3.46 Å

[a]Substrate temperature.
[b]Chamber pressure.
[c]Measured by QCM.
[d]Measured by XRR.

not all of the incoming Ir atoms were oxidized to form IrO_2 during growth. Furthermore, Samples 1 and 2 had little to no indication of the rutile IrO_2 phase present in the XRD $2\theta - \omega$ scan. This suggests that although the substrate temperature of 400 °C is predicted to be within the growth window, this temperature does not enable complete oxidation of Ir to IrO_2. Sample 3, which was grown at 300 °C and a higher Ir flux, also appears to have some intensity due to Ir 111. The 0006 peak of another phase, α-Ir_2O_3, would be expected at 39.92°.[43] However, according to previous literature, α-Ir_2O_3 is unlikely to form at MBE growth conditions or on the (110) TiO_2 surface. The peak at 40.75° is more closely aligned to the metallic Ir 111 at 40.55°, which we expect in the event of incomplete oxidation of Ir to the rutile phase. Samples 4–7 appear phase pure in the $2\theta - \omega$ scan. All samples except Samples 1 and 2 had IrO_2 110 and 220 peaks. This supports our conclusion that a substrate temperature of 300 °C is within the growth window, but 400 °C is too hot to grow phase pure films of IrO_2.

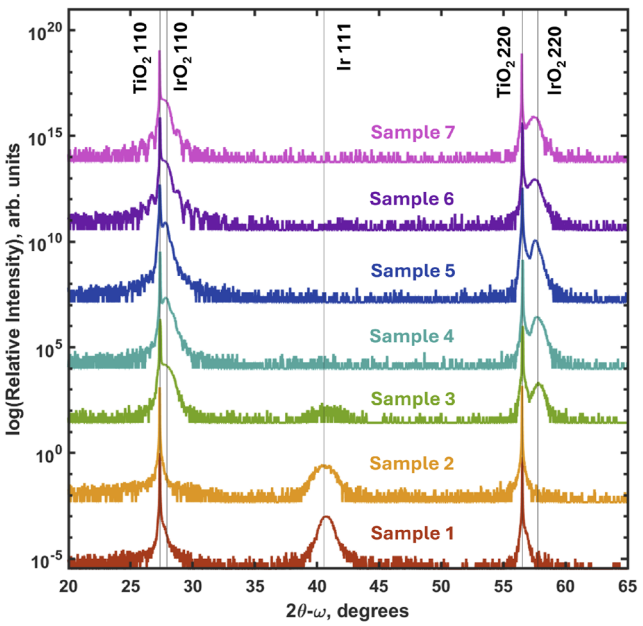

FIG. 3. XRD $2\theta - \omega$ scans of all samples. The relative intensity is plotted on a logarithmic scale.

D. Growth kinetics

RHEED patterns were collected along either the [001] or [1$\bar{1}$0] zones for all samples. The RHEED data for all of the samples are compiled in Fig. 4. Patterns from Samples 1–4 indicated crystalline films with noticeable surface roughness. Samples 5–7 had thin, streaky RHEED patterns without apparent roughness, supporting XRD observations of higher crystallinity in these films. AFM images of Samples 5–7 reveal the presence of grains and suggest the Volmer–Weber growth mode is dominant (Fig. 5). This is consistent with pulsed laser deposition studies that have shown island growth dominates in the initial layers of epitaxial (110) IrO_2 films due to high mismatch with the TiO_2 substrate.[44] The raised linear regions on the surface of Sample 5 were found to be parallel to the [001] direction. Similar features have been observed previously in rutile films[11,17] and are attributed to high in-plane strain that leads to cracking.

E. Film quality

Overall, films grown at low-flux and low-pressure had the highest crystalline quality, with Sample 6 identified as the highest-quality sample with the lowest RMS roughness. The crystalline and epitaxial quality of Sample 6 was more thoroughly characterized by STEM and XRD (Figs. 6 and 7). The STEM high angle annular dark field (HAADF) images in Fig. 6(a) showed hundreds of nanometers along the surface of Sample 6 without surface features, interfacial features, or second phases. Higher-resolution images of Sample 6 [Figs. 6(b) and 6(c)] demonstrated the presence of atomic step edges along the film surface and continuous epitaxial alignment across the substrate-film interface. STEM EDS (supplementary material Fig. 4) characterized the chemical composition across the film, indicating a relatively sharp substrate/film interface (≈2 nm) and that the film

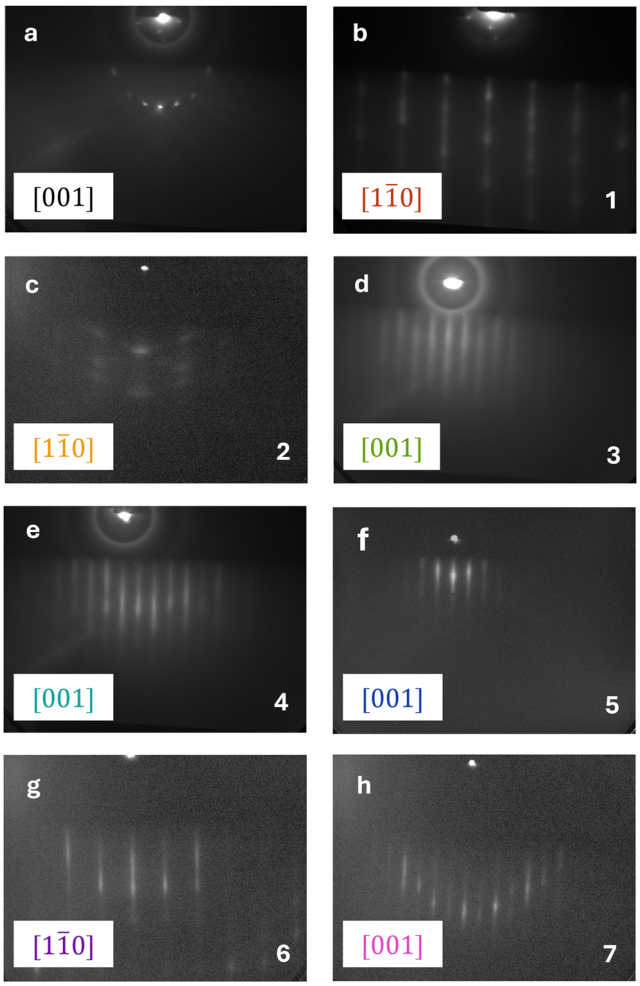

FIG. 4. RHEED patterns of (a) a representative substrate and [(b)–(h)] Samples 1–7, respectively.

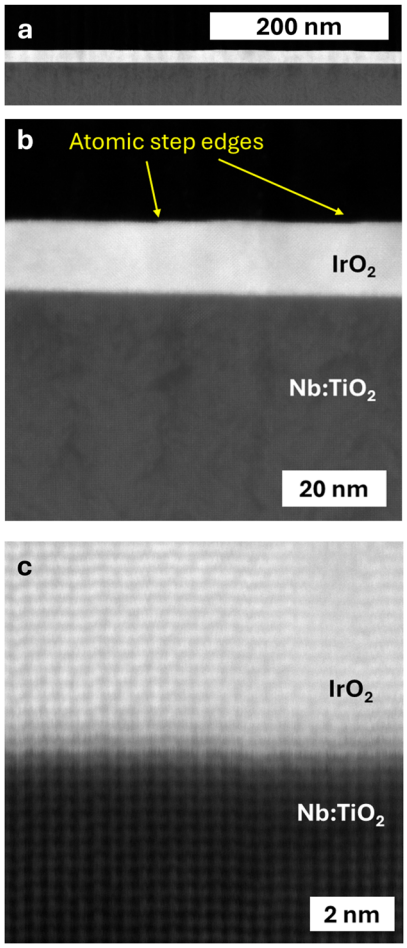

FIG. 6. (a) STEM HAADF survey image of Sample 6. (b) HAADF images of Sample 6 indicating atomic step edges on the film surface. (c) Atomic resolution HAADF images of the substrate-film interface in Sample 6.

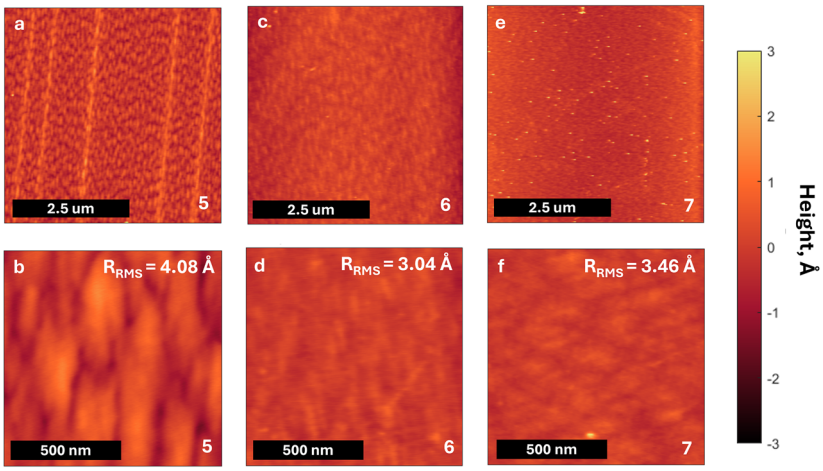

FIG. 5. AFM images and calculated RMS roughness values of the surface of [(a) and (b)] Sample 5, [(c) and (d)] Sample 6, and [(e) and (f)] Sample 7.

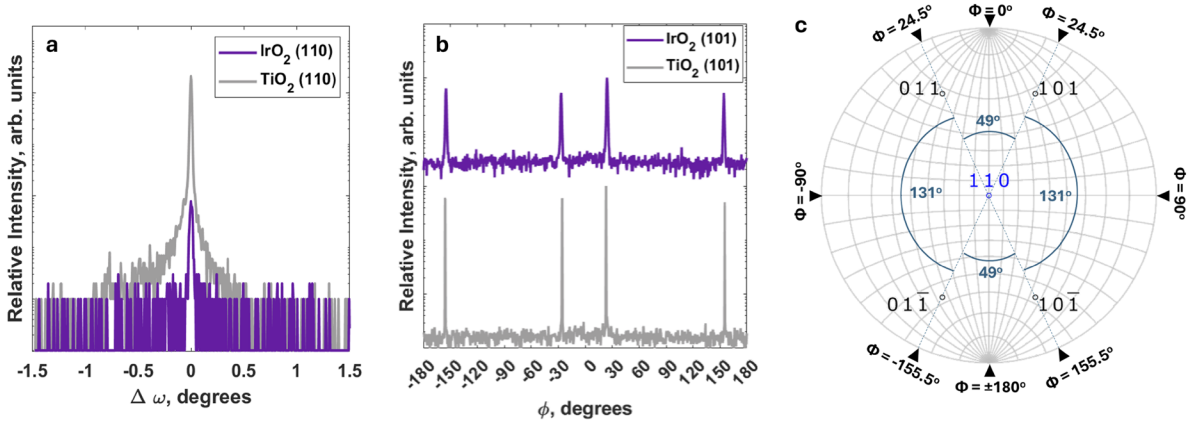

FIG. 7. (a) ω-scan of Sample 6 demonstrating low-mosaicity of the film. (b) ϕ-scan of Sample 6 demonstrating in-plane epitaxial orientation. (c) Stereographic projection explaining peak spacing in ϕ scan.

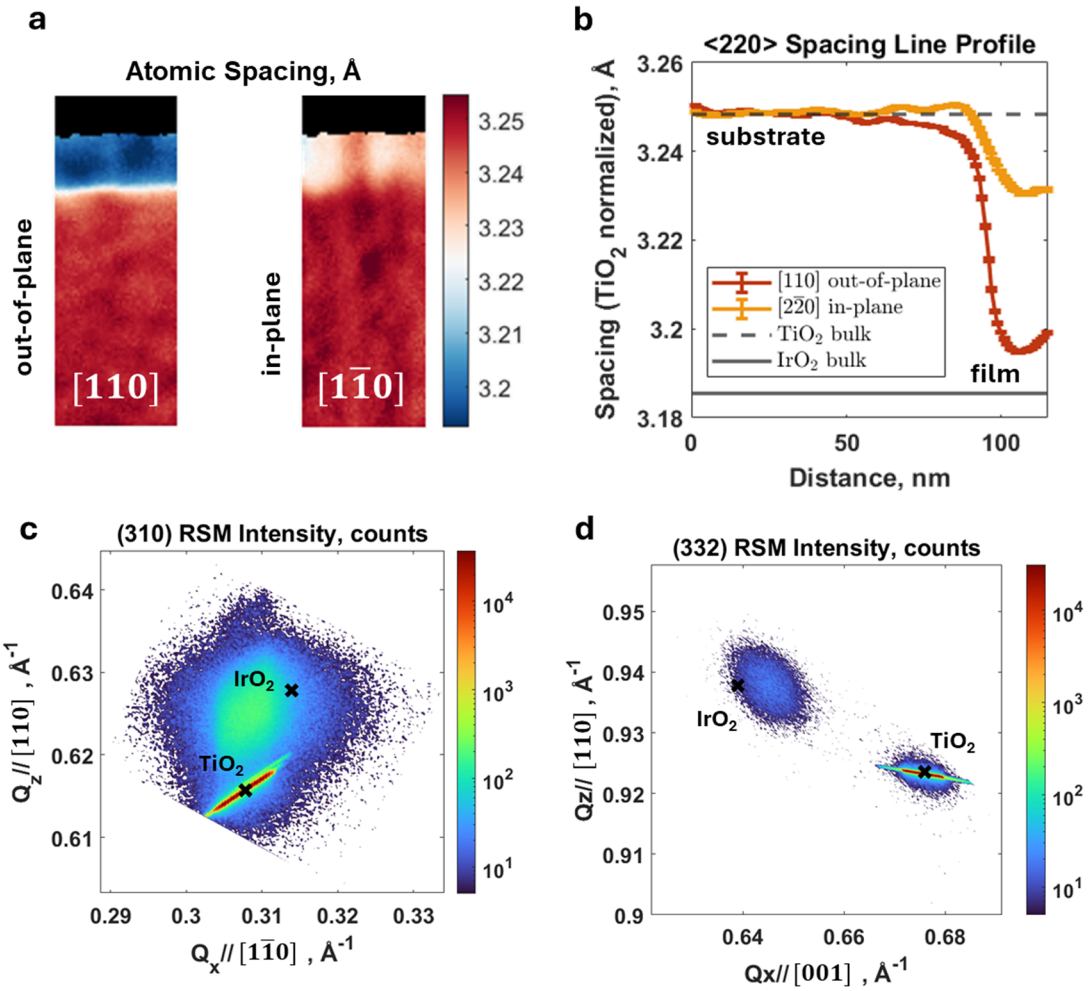

FIG. 8. (a) Interatomic distance mapping for Sample 6, (b) line profiles for atomic spacing across the substrate-film interface in the in-plane and out-of-plane directions, [(c) and (d)] RSM collected to determine the average strain in the [001] and [1$\bar{1}$0] in-plane directions.

and substrate had similar oxygen content, as expected for a fully oxidized film. The rocking curve measured in the XRD ω-scan in Fig. 7(a) revealed a low FWHM of the film (0.030°) relative to the substrate FWHM (0.015°). A slight asymmetry is noted in the peak that was dependent on the slit size of the detector and is attributed to an instrument artifact. The ϕ-scan of Sample 6 [Fig. 7(b)] established the epitaxial in-plane alignment of Sample 6.

F. Strain

In-plane and out-of-plane strain in Sample 6 was characterized by RSM and 4D-STEM, as shown in Fig. 8. 4D-STEM allows direct measurement of lattice parameters from nanoscale regions of the sample, while RSM provides averaged information due to the millimeter-scale x-ray probe. Rutile TiO_2 has a larger a lattice parameter and a smaller c lattice parameter than IrO_2. The STEM data were taken along the c direction, with the [110] direction out-of-plane and the [1$\bar{1}$0] direction in-plane. We observe a partially relaxed film, with strain in the in-plane direction of 1.41% by STEM and 1.59% by RSM compared to relaxed IrO_2. This corresponds to a nearly relaxed out-of-plane lattice parameter (0.39% by STEM or 0.44% by RSM). The only measurement of strain in the [001] direction was from RSM, which indicated a compressed lattice parameter of −2.02%. 4D-STEM did not measure strain in the [001] direction because the lamella prepared for 4D-STEM was oriented along the [001] zone during data collection. Overall, the strain measurements (tabulated in the supplementary material, Table 1) were in good agreement across techniques and compared to the literature.[8,12–17,44]

G. Comparison of IrO_2 reactive MBE growth methods

We compared film quality and relaxation behavior with respect to growth method with data from the literature. Reported surface roughness values taken from the literature indicate that OAMBE produces the smoothest films (R_{RMS} = 0.7 Å),[8] followed by MOMBE (R_{RMS} = 1.073 Å)[17] and PAMBE (R_{RMS} = 3.04 Å). Films grown with OAMBE have significantly lower FWHM (0.005°),[14,15,45] whereas the reported rocking curves of MOMBE IrO_2 are comparable to PAMBE (0.1°-0.2°).[17] The films compared across literature were grown at different thicknesses but appear to have similar trends in strain and relaxation. We note that final film roughness and film mosaicity are also dependent on original substrate quality, substrate miscut, and post-growth treatments. A more controlled experiment is required to make an accurate comparison of final film quality and relaxation behavior with respect to growth method.

IV. CONCLUSION

Here, we have shown that it is possible to grow high-quality epitaxial films of IrO_2 using an oxygen plasma as the sole oxidant. Investigation into the plasma composition reveals it to be dominated by atomic oxygen. We have calculated the thermodynamic equilibria between Ir and IrO_2 in the presence of O_2 and O. This new approach to IrO_2 film growth expands the number of possible techniques that can be used to synthesize IrO_2 films for study in a variety of key applications.

SUPPLEMENTARY MATERIAL

The supplementary material includes derivations of the Ellingham diagram relationships and the linear regression plots of the $\Delta G^o_{f,\ IrO_2}$ and $\Delta G^o_{f,\ O}$. XRD of the Kiessig and Laue fringes of all the samples is included with the film thicknesses calculated from these scans. The supplementary material also contains additional EDS and 4D-STEM data.

ACKNOWLEDGMENTS

The authors would like to acknowledge D. Drury, S. Schaefer, B. Tellekamp, D. M. Febba, and A. Zakutayev for assistance in collecting the OES measurements and V. Stevanovic and C. Wolden for useful discussions. Additional acknowledgments to B. Tellekamp for assistance with XRD measurement. Some of the work was performed in the Colorado School of Mines' Shared Instrumentation Facility, including the Core Facilities for Electron Microscopy (RRID:SCR_022048), Scanning Probe and Optical Microscopy (RRID:SCR_022048), and X-ray Diffraction and Computed Tomography (RRID:SCR_022053). This work was authored in part by the National Renewable Energy Laboratory for the U.S. Department of Energy (DOE) under Contract No. DE-AC36-08GO28308. The views expressed in the article do not necessarily represent the views of the DOE or the U.S. Government.

AUTHOR DECLARATIONS

Conflict of Interest

The authors have no conflicts to disclose.

Author Contributions

D. Sacksteder: Conceptualization (equal); Investigation (equal); Methodology (equal); Visualization (equal); Writing – original draft (equal); Writing – review & editing (equal). **S. C. Dahl**: Investigation (equal); Writing – review & editing (equal). **J. Dorsey**: Investigation (equal). **K. Yazawa**: Investigation (equal); Writing – review & editing (equal). **M. E. Holtz**: Conceptualization (equal); Funding acquisition (lead); Investigation (equal); Methodology (equal); Resources (equal); Supervision (equal); Validation (equal); Writing – review & editing (equal).

DATA AVAILABILITY

The data that support the findings of this study are available from the corresponding author upon reasonable request.

REFERENCES

[1] H.-J. Cho, H. Horii, C. S. Hwang, J.-W. Kim, C. S. Kang, B. T. Lee, S. I. Lee, Y. B. Koh, and M. Y. Lee, "Preparation and characterization of iridium oxide thin films grown by DC reactive sputtering," Jpn. J. Appl. Phys. **36**, 1722 (1997).

[2] C. U. Pinnow, I. Kasko, C. Dehm, B. Jobst, M. Seibt, and U. Geyer, "Preparation and properties of DC-sputtered IrO_2 and Ir thin films for oxygen barrier applications in advanced memory technology," J. Vac. Sci. Technol. B **19**, 1857–1865 (2001).

[3]L. Trupina, C. Miclea, L. Amarande, and M. Cioangher, "Growth of highly oriented iridium oxide bottom electrode for Pb(Zr,Ti)O_3 thin films using titanium oxide seed layer," J. Mater. Sci. **46**, 6830 (2011).
[4]C. U. Pinnow, I. Kasko, N. Nagel, S. Poppa, T. Mikolajick, C. Dehm, W. Hösler, F. Bleyl, F. Jahnel, M. Seibt, U. Geyer, and K. Samwer, "Influence of deposition conditions on Ir/IrO_2 oxygen barrier effectiveness," J. Appl. Phys. **91**, 9591–9597 (2002).
[5]J. Y. Chen, Y. M. Chen, Y. Sun, J. F. Lee, S. Y. Chen, P. C. Chen, and P. W. Wu, "Chemical bath deposition of IrO_2 films on ITO substrate," Ceram. Int. **40**, 14983–14990 (2014).
[6]V. Di Palma, A. Pianalto, M. Perego, G. Tallarida, D. Codegoni, and M. Fanciulli, "Plasma-assisted atomic layer deposition of IrO_2 for neuroelectronics," Nanomaterials **13**, 976 (2023).
[7]D. D. Matienzo, D. Settipani, E. Instuli, and T. Kallio, "Active IrO_2 and NiO thin films prepared by atomic layer deposition for oxygen evolution reaction," Catalysts **10**, 92 (2020).
[8]J. N. Nelson, J. P. Ruf, Y. Lee, C. Zeledon, J. K. Kawasaki, S. Moser, C. Jozwiak, E. Rotenberg, A. Bostwick, D. G. Schlom, K. M. Shen, and L. Moreschini, "Dirac nodal lines protected against spin–orbit interaction in IrO_2," Phys. Rev. Mater. **3**, 064205 (2019).
[9]S. Schlicht, S. Haschke, V. Mikhailovskii, A. Manshina, and J. Bachmann, "Highly reversible water oxidation at ordered nanoporous iridium electrodes based on an original atomic layer deposition," ChemElectroChem **5**, 1259 (2018).
[10]K. A. Stoerzinger, L. Qiao, M. D. Biegalski, and Y. Shao-Horn, "Orientation-dependent oxygen evolution activities of rutile IrO_2 and RuO_2," J. Phys. Chem. Lett. **5**, 1636–1641 (2014).
[11]J. P. Ruf, H. Paik, N. J. Schreiber, H. P. Nair, L. Miao, J. K. Kawasaki, J. N. Nelson, B. D. Faeth, Y. Lee, B. H. Goodge, B. Pamuk, C. J. Fennie, L. F. Kourkoutis, D. G. Schlom, and K. M. Shen, "Strain-stabilized superconductivity," Nat. Commun. **12**, 59 (2021).
[12]S. Nair, Z. Yang, K. Storr, and B. Jalan, "High-mobility carriers in epitaxial IrO_2 films grown using hybrid molecular beam epitaxy," Nano Lett. **24**, 10850 (2024).
[13]A. Bose, J. N. Nelson, X. S. Zhang, P. Jadaun, R. Jain, D. G. Schlom, D. C. Ralph, D. A. Muller, K. M. Shen, and R. A. Buhrman, "Effects of anisotropic strain on spin–orbit torque produced by the Dirac nodal line semimetal IrO_2," ACS Appl. Mater. Interfaces **12**, 55411–55416 (2020).
[14]J. K. Kawasaki, C. H. Kim, J. N. Nelson, S. Crisp, C. J. Zollner, E. Biegenwald, J. T. Heron, C. J. Fennie, D. G. Schlom, and K. M. Shen, "Engineering carrier effective masses in ultrathin quantum wells of IrO_2," Phys. Rev. Lett. **121**, 176802 (2018).
[15]J. K. Kawasaki, M. Uchida, H. Paik, D. G. Schlom, and K. M. Shen, "Evolution of electronic correlations across the rutile, perovskite, and Ruddelsden-Popper iridates with octahedral connectivity," Phys. Rev. B **94**, 121104 (2016).
[16]M. Uchida, W. Sano, K. S. Takahashi, T. Koretsune, Y. Kozuka, R. Arita, Y. Tokura, and M. Kawasaki, "Field-direction control of the type of charge carriers in nonsymmorphic IrO_2," Phys. Rev. B **91**, 241119 (2015).
[17]S. Nair, Z. Yang, D. Lee, S. Guo, J. T. Sadowski, S. Johnson, A. Saboor, Y. Li, H. Zhou, R. B. Comes, W. Jin, K. A. Mkhoyan, A. Janotti, and B. Jalan, "Engineering metal oxidation using epitaxial strain," Nat. Nanotechnol. **18**, 1005–1011 (2023).
[18]S.-W. Kim, S.-H. Kwon, D.-K. Kwak, and S.-W. Kang, "Phase control of iridium and iridium oxide thin films in atomic layer deposition," J. Appl. Phys. **103**, 023517 (2008).
[19]J. Hämäläinen, T. Hatanpää, E. Puukilainen, T. Sajavaara, M. Ritala, and M. Leskelä, "Iridium metal and iridium oxide thin films grown by atomic layer deposition at low temperatures," J. Mater. Chem. **21**, 16488 (2011).
[20]W. Tan, O. L. Hendricks, A. C. Meng, M. R. Braun, M. D. McGehee, C. E. D. Chidsey, and P. C. McIntyre, "Atomic layer deposited TiO_2–IrO_x alloy as a hole transport material for perovskite solar cells," Adv. Mater. Interfaces **5**, 1800191 (2018).
[21]A. M. Torres-Huerta, J. R. Vargas-García, and M. A. Domínguez-Crespo, "Preparation and characterization of IrO_2–YSZ nanocomposite electrodes by MOCVD," Solid State Ionics **178**, 1608–1616 (2007).
[22]M. A. El Khakani and M. Chaker, "Reactive pulsed laser deposition of iridium oxide thin films," Thin Solid Films **335**, 6–12 (1998).
[23]X. Hou, R. Takahashi, T. Yamamoto, and M. Lippmaa, "Microstructure analysis of IrO_2 thin films," J. Cryst. Growth **462**, 24–28 (2017).
[24]W. J. Kim, E. K. Ko, S. Y. Kim, B. Kim, and T. W. Noh, "In-operando spectroscopic ellipsometry studies of IrO_2 dynamic instabilities: Guide to in-situ growth of pyrochlore iridate thin films," Curr. Appl. Phys. **19**, 400–405 (2019).
[25]S. Ardizzone, C. L. Bianchi, L. Borgese, G. Cappelletti, C. Locatelli, A. Minguzzi, S. Rondinini, A. Vertova, P. C. Ricci, C. Cannas, and A. Musinu, "Physico-chemical characterization of IrO_2–SnO_2 sol-gel nanopowders for electrochemical applications," J. Appl. Electrochem. **39**, 2093 (2009).
[26]Z. Novotny, B. Tobler, L. Artiglia, M. Fischer, M. Schreck, J. Raabe, and J. Osterwalder, "Kinetics of the thermal oxidation of Ir(100) toward IrO_2 studied by ambient-pressure x-ray photoelectron spectroscopy," J. Phys. Chem. Lett. **11**, 3601–3607 (2020).
[27]D.-Y. Kuo, J. K. Kawasaki, J. N. Nelson, J. Kloppenburg, G. Hautier, K. M. Shen, D. G. Schlom, and J. Suntivich, "Influence of surface adsorption on the oxygen evolution reaction on IrO_2(110)," J. Am. Chem. Soc. **139**, 3473 (2017).
[28]D. G. Schlom, "Perspective: Oxide molecular-beam epitaxy rocks!," APL Mater. **3**, 062403 (2015).
[29]J. N. Nelson, "Revealing the electronic structure of iridates with light and how it can be controlled through epitaxy," Ph.D. Thesis (Cornell University, 2020).
[30]S.-L. Shang, S. Lin, M. C. Gao, D. G. Schlom, and Z.-K. Liu, "Ellingham diagrams of binary oxides," APL Mater. **12**, 081110 (2024).
[31]E. A. Clinton, E. Vadiee, M. B. Tellekamp, and W. A. Doolittle, "Observation and mitigation of RF-plasma-induced damage to III-nitrides grown by molecular beam epitaxy," J. Appl. Phys. **126**, 015705 (2019).
[32]A. Kramida, Y. Ralchenko, J. Reader, and NIST ASD Team, *NIST Atomic Spectra Database, Version 5.12* (National Institute of Standards and Technology, 2024), https://physics.nist.gov/asd.
[33]K. M. Adkison, S.-L. Shang, B. J. Bocklund, D. Klimm, D. G. Schlom, and Z.-K. Liu, "Suitability of binary oxides for molecular-beam epitaxy source materials: A comprehensive thermodynamic analysis," APL Mater. **8**, 081110 (2020).
[34]M. W. J. Chase, C. Davies, R. J. Downey, D. J. Frurip, R. A. McDonald, and A. N. Syverud, *NIST JANAF Database of Thermochemical Tables* (National Institute of Standards and Technology, 2013), https://janaf.nist.gov.
[35]P. Eaton and P. West, *Atomic Force Microscopy* (Oxford University Press, 2010), pp. 104–108.
[36]E. Padgett, M. E. Holtz, P. Cueva, Y.-T. Shao, E. Langenberg, D. G. Schlom, and D. A. Muller, "The exit-wave power-cepstrum transform for scanning nanobeam electron diffraction: Robust strain mapping at subnanometer resolution and subpicometer precision," Ultramicroscopy **214**, 112994 (2020).
[37]F. Rezaei, M. Abbasi-Firouzjah, and B. Shokri, "Investigation of antibacterial and wettability behaviours of plasma-modified PMMA films for application in ophthalmology," J. Phys. D: Appl. Phys. **47**, 085401 (2014).
[38]K. Farhadian-Azizi, M. Abbasi-Firouzjah, M. Abbasi, and M. Hashemzadeh, "Optical monitoring of DC/RF plasma sputtering for copper oxide film growth at low temperature," Surf. Interfaces **40**, 103007 (2023).
[39]M. Abbasi-Firouzjah, S. I. Hosseini, M. Shariat, and B. Shokri, "The effect of TEOS plasma parameters on the silicon dioxide deposition mechanisms," J. Non-Cryst. Solids **368**, 86–92 (2013).
[40]H. Carrère, A. Arnoult, A. Ricard, and E. Bedel-Pereira, "RF plasma investigations for plasma-assisted MBE growth of (Ga,In)(As,N) materials," J. Cryst. Growth **243**, 295–301 (2002).
[41]H. P. Nair, Y. Liu, J. P. Ruf, N. J. Schreiber, S.-L. Shang, D. J. Baek, B. H. Goodge, L. F. Kourkoutis, Z.-K. Liu, K. M. Shen, and D. G. Schlom, "Synthesis science of $SrRuO_3$ and $CaRuO_3$ epitaxial films with high residual resistivity ratios," APL Mater. **6**, 046101 (2018).
[42]Y. Krockenberger, J. Kurian, A. Winkler, A. Tsukada, M. Naito, and L. Alff, "Superconductivity phase diagrams for the electron-doped cuprates

$R_{2-x}Ce_xCuO_4$ (R = La, Pr, Nd, Sm, and Eu)," Phys. Rev. B **77**, 060505 (2008).
[43]J. G. Hao, H. H. Gong, X. H. Chen, Y. Xu, F. F. Ren, S. L. Gu, R. Zhang, Y. D. Zheng, and J. D. Ye, "*In situ* heteroepitaxial construction and transport properties of lattice-matched α-Ir_2O_3/α-Ga_2O_3 p-n heterojunction," Appl. Phys. Lett. **118**, 261601 (2021).
[44]P. Keßler, T. Waldsauer, V. Jovic, M. Kamp, M. Schmitt, M. Sing, R. Claessen, and S. Moser, "Epitaxial RuO_2 and IrO_2 films by pulsed laser deposition on TiO_2(110)," APL Mater. **12**, 101110 (2024).
[45]J. K. Kawasaki, D. Baek, H. Paik, H. P. Nair, L. F. Kourkoutis, D. G. Schlom, and K. M. Shen, "Rutile IrO_2/TiO_2 superlattices: A hyperconnected analog to the Ruddelsden-Popper structure," Phys. Rev. Mater. **2**, 054206 (2018).